Confocal fluorescence correlation spectroscopy through a sparse layer of scattering objects

Anirban Sarkar, Joseph Gallagher, Irène Wang, Giovanni Cappello, Jörg Enderlein, Antoine Delon, Jacques Derouard

HAL Id: hal-02346996

https://hal.science/hal-02346996

Submitted on 5 Nov 2019

Confocal fluorescence correlation spectroscopy through a sparse layer of scattering objects

Anirban Sarkar,[1] **Joseph Gallagher,**[1,2] **Irène Wang,**[1] **Giovanni Cappello,**[1] **Jörg Enderlein,**[3] **Antoine Delon,**[1,*] **and Jacques Derouard**[1]

[1]*Univ. Grenoble Alpes, CNRS, LIPhy, 38000 Grenoble, France*
[2]*Alpao SAS, Inovallée, 345 rue Lavoisier, 38330 Montbonnot Saint-Martin, France*
[3]*Third Institute of Physics – Biophysics, Georg August University, 37077 Göttingen, Germany*
*antoine.delon@univ-grenoble-alpes.fr

Abstract: In the presence of strong light scattering, as often encountered in biological tissue, optical microscopy becomes challenging and technical demanding. Beside image quality, the quantitative determination of molecular properties is also strongly affected by scattering. We have carried out fluorescence correlation spectroscopy (FCS) experiments, in a solution of fluorophores, through a sparse scattering layer made of dielectric beads. We observe that the fluorescence signal steadily decreases as the focus is moved away from the scattering layer. By contrast, the estimated number of molecules recovers its normal value beyond a characteristic distance of about twice the bead diameters, below which it is strongly biased. Accompanying theoretical modeling demonstrates how diffraction and refraction by the scattering layer and their impact on FCS measurements depend on size and refractive index of the beads.

1. Introduction

Fluorescence Correlation Spectroscopy (FCS) is a widely used technique to measure the absolute concentration, dynamics and mobility of molecules (in the pM to µM range) in various environments, including complex biological media [1–3]. It uses the temporal autocorrelation function (ACF) of the fluorescence signal collected within a small detection volume of a sample with a confocal microscope. A least square fit of the ACF provides parameters such as the number of molecules within the detection volume and the diffusion time in and out of this volume. These quantities are thus sensitive to the size and shape of this detection volume, quantitatively defined by the Molecular Detection Function (MDF) that can be approximated by the product of the excitation light intensity distribution and the fluorescence collection efficiency [3]. However, both these functions are affected by the optical aberrations and light scattering that may occur when observing inhomogeneous samples. As a matter of fact, Leroux *et al* have shown experimentally that FCS measurements are strongly biased when observing through a single living cell [4] or inside a living spheroid [5], although part of this bias may be corrected using adaptive optics [5]. FCS measurements in a model turbid medium (suspension of polystyrene beads) have been performed by Zustiak *et al* [6] who have observed a significant decrease in the molecular brightness together with an increase in the molecule number. These observations were attributed to a loss of ballistic photons and to an enlargement of the detection volume, caused by the scattering of the excitation light by the turbid sample. In fact, the fluorescence emitted by the molecules is also affected by scattering, which induces an additional decrease in the molecular brightness and an increase in the molecular number.

From a theoretical point of view, the description of these effects requires to model the propagation of light in a turbid medium. To do this, many theoretical studies utilize Monte Carlo method [7–11], assuming a random model for the turbid medium and some angular distribution of the light scattered by the particles, neglecting most of the time the coherence of light. Actually, an exact computation of the propagation of the electromagnetic field, such as the FDTD method, through a complex and thick medium would be extremely costly though some interesting alternatives have been proposed [12]. In addition, computing the exact epifluorescence signal generated within the aberrated excitation focus is even more difficult.

The situation is much simpler when the turbid medium is reduced to a thin, static, scattering layer. This is the situation we study in the present paper. The aim of the present work is to understand how fluorescence measurements in a clear solution of fluorophores observed through a scattering layer depend on the optical characteristics of the particles that compose this scattering layer and also how they depend on the distance between the excitation focus and the scattering layer. More specifically, FCS measurements give access, in addition to the fluorescence count rate, to the size of the detection volume (proportional to the number of molecules). We shall see how these quantities are affected by light scattering. Moreover, although the shape of the detection volume can be inferred from the temporal behavior of the autocorrelation function, the limited experimental S/N prevents such an analysis. Several types of scattering layers are used, all composed of dielectric beads deposited on a coverslip. The samples differ by size, coverage fraction of the substrate, and refractive index of the beads.

In order to interpret the measurements, we have carried out numerical simulations of the experiments using a scalar wave description of the propagation of excitation and fluorescence light to compute the MDF of the set-up, from which the fluorescence detection intensity and the detection volume could be calculated.

2. Material and methods

2.1 Sample preparation

Silica beads (3.34 ± 0.14, 6.12 ± 0.20 and 15.29 ± 0.49 µm in diameter, refractive index 1.458 at 590 nm), hereafter called 3, 6 and 15 µm silica beads, were purchased from microParticles GmbH. To immobilize the silica beads on the surface, Lab-Tek coverglass #1 (Thermo Fisher Scientific) was treated with plasma and UV, before covering the surface with 30 µL of Poly-lysine solution (0.1 w/v Sigma-Aldrich). After solvent evaporation, dispersed beads were poured into a Lab-Tek well containing a PBS solution of $\cong 20$ nM Sulforhodamine B (SRB) sodium salt (Sigma-Aldrich), to reach a coverage fraction of the surface ranging from less than 10% to more than 25%, as schematically shown in Fig. 1.

Polydispersed polyacrylamide beads (PAA, 14.5 ± 3.6 µm in diameter, refractive index 1.349 at 589nm according to measurements performed on beads of similar properties [13]) were fabricated using a water-in-oil emulsion approach, as described elsewhere [14]. Very briefly, an emulsion of an acrylamide/bisacrylamide mix is formed in oil, using HFE 7500 perfluorinated oil (3M) with PFPE-PEG surfactant (kindly provided by Prof. Garstecki). Initiator TEMED, oxidizing agent APS and acrylic acid (all from Sigma Aldrich) have been used as usual. Special attention has been paid to degas the solutions using vacuum chamber before vortexing the whole mixture to produce droplets (diameter from below 10 µm to tens of µm). We kept emulsion under argon atmosphere during polymerisation at 60°C for 1h50. To transfer beads into aqueous solution, PBS was gently added to the emulsion with a subsequent addition of 400 µL of 1H, 2H, 2H-perfluorooctanol (Sigma-Aldrich). These beads were added to the 20 nM SRB solution and slowly sank to the bottom of the Lab-Tek well before immobilization.

Latex beads of refractive index 1.59 (3, 6 and 15 µm diameter, Sigma-Aldrich) were used for complementary experiments.

2.2 Experimental set-up and data analysis

Our experimental set-up is based on a custom built confocal microscope, controlled with Matlab (Mathworks). The output of a 561 nm-diode pumped solid state laser (Cobolt) is directed to galvanometric mirrors used for scanning (6215H, Cambridge technology), before reaching the microscope base (Olympus IX71) where it is focused by the objective (Zeiss, water-immersion, 63 × , NA = 1.2). A dichroic mirror (Chroma ZT561rdc) and an emission filter (ET577.5lp) filter out the excitation light from the fluorescence emission, which is detected by an avalanche photodiode (APD, SPCM-AQRH-13, Perkin Elmer) through a multimode fiber that acts as a pinhole with diameter 0.7 times that of the diffraction-limited spot. The pulses delivered by the APD are sent to a data acquisition board (PCIe-6321, National Instrument) that counts events during periods of 1 µs.

Three time series of 20 s were recorded per FCS measurement, providing a mean value and an error of the autocorrelation curve, calculated using Matlab (Mathworks). The acquisitions were performed on a X,Y,Z grid to sample the FCS measurements above the substrate (Fig. 1). The X,Y-coordinates (typically 20), corresponding to different bead configurations, were chosen randomly within a squared surface of $c.a.$ 100×100 µm^2. We took care to exclude positions right at the vertical of beads, because they lead to abnormal autocorrelation curves that cannot be fit to estimate reliable numbers of molecules.
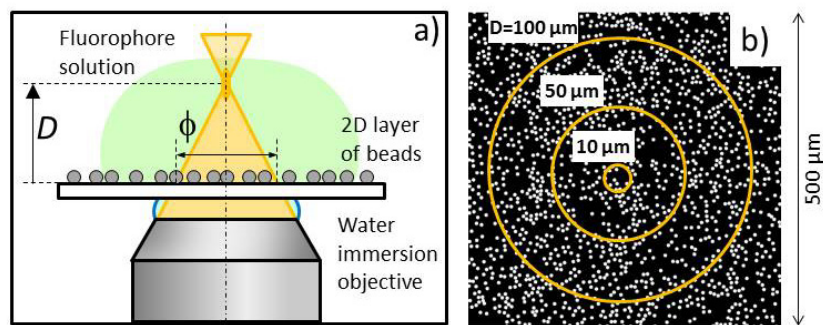

Fig. 1. a) Scheme of the optical configuration, showing the illumination and detection beams scattered by the 2D layer of beads within a disk of diameter ϕ, which depends upon the observation depth, D; b) segmented image of a 2D layer of beads with coverage fraction 17%, where the superimposed circles correspond to observation depths, D = 10, 50 and 100 µm.

For each pair of X,Y-coordinates, a series of 20 measurements were performed from the surface up to 100 µm in depth, by steps increasing from 1 µm to 20 µm. For each sample, a mosaic confocal image of the beads covering a total surface of $ca.$ 500×500 µm^2 was recorded around the region where the FCS measurements were taken. Given the angular aperture of the laser beam ($2 \times 64.5°$), the bead configuration intersected by the excitation and emitted beams could be recovered, as the focus was moved up to 100 µm deep.

The autocorrelation curves were eventually fitted with the standard 3D diffusion model [1], the relevant parameters of which are the effective diffusion time, τ_D and the number of molecules, N, in addition to the total count rate, CR (this latter is independent of the fit). As the diffusion time is model dependent, we disregard it in this work, because its analysis would require a detailed 3D description of the detection volume that is far beyond our goal. The count rate is proportional to the number of molecules in the detection volume times their brightness, while the number of molecules solely depends upon the detection volume (the molecular concentration being constant). We now describe the theoretical and numerical approach used to calculate the CR and N metrics.

2.3 Numerical simulations

2.3.1 Scalar, angular spectrum model

The numerical simulations are based on the propagation of a spherical wave after it passes through a scattering substrate composed of dielectric beads deposited at random on a coverslip.

To do this we use a scalar model for the wave, which ignores polarization effects. We think this is a good approximation for two reasons: i) We are concerned by the scattering of light by particles that are large (a few µm) compared to the wavelength (0.56 µm in vacuum, 0.42µm in water). Under these conditions the difference between the scattering diagrams in planes parallel and perpendicular to the polarization of incoming wave is small, as can be shown using exact Mie theory [15]; ii) Although in our experimental conditions the numerical aperture of the microscope objective is relatively large (NA = 1.2) we have checked that the relative difference in focus size parallel and perpendicular to the polarization of the incoming wave is small, performing calculations using the exact Richards and Wolf model [16]; it also appears that the excitation polarization in the focus place is mostly parallel to the incoming one; iii) regarding fluorescence emission, as the molecules rotate faster than their lifetime, the anisotropy of their radiation pattern is expected to vanish.

The propagation of this scalar wave is described using the angular spectrum representation of optical field [17]. The complex amplitude of the wave, in a plane at position z along the direction of propagation of the beam, is decomposed into a 2D Fourier space k_x, k_y that can be associated to a plane wave of wavelength λ with propagation vector components k_x, k_y, $k_z = (k^2 - k_x^2 - k_y^2)^{1/2}$ where $k = 2\pi/\lambda$. Then, the wave at any point beyond this plane is a superposition of these plane waves that propagate in free space from the initial plane to the plane of interest ($k^2 - k_x^2 - k_y^2 < 0$ corresponds to evanescent waves that vanish at distances larger than a few wavelengths from the initial plane).

The calculation of the FCS signal, obtained when focusing the laser beam at a distance Z behind the scattering layer, is carried out according to the scheme shown in Fig. 2.
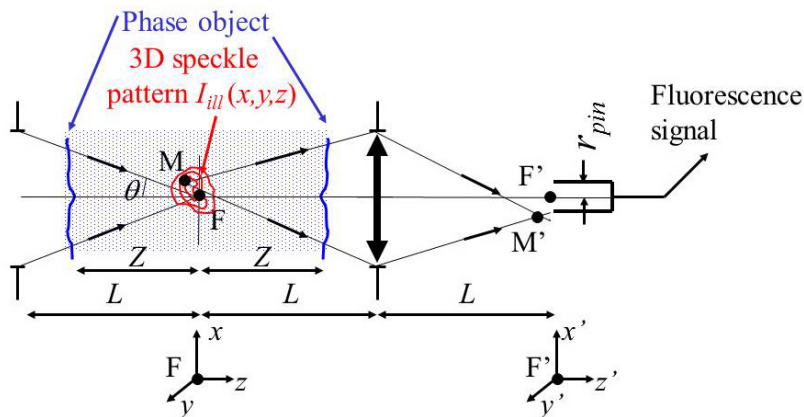

Fig. 2. Scheme of the illumination and fluorescence collection optics used in the numerical modelling

The wave transmitted by this layer, described by a phase object of complex transmittance $T_\Phi(x,y)$, reads $A(x,y,-Z) \times T_\Phi(x,y)$, where $A(x,y,-Z)$ represents the incident laser beam focused at the origin, F, of the z axis. Eventually, this wave propagates through the solution. Each SRB molecule at position $M(x_0,y_0,z_0)$ excited by the incident light emits fluorescence represented by a diverging spherical wave $A_{em}(x_0,y_0,z_0;x,y,z)$. For the modeling it is more convenient to consider transmission geometry as depicted in Fig. 2, rather than an

epifluorescence one. Therefore, analogous to the excitation path, the emitted fluorescence also passes through a replica of the scattering layer after which the wave can be expressed as $A_{em-tr} = A_{em}(x_0, y_0, z_0; x, y, Z) \times T_{\Phi}(x, y)$. Afterwards, this wave propagates up to the collection optics described by a converging lens of focal length $L/2$, with a complex transmittance $T_{coll}(x,y)$. Finally the transmitted wave propagates up to the plane of the pinhole located at F', which is the image of F by the collecting optics.

2.3.2 Primary excitation beam

Experimentally, the sample is illuminated by a laser beam which Gaussian profile overfills by far the aperture of the microscope objective. This incident beam is thus described by a truncated spherical wave which amplitude, at a point $x, y, -L$ of the aperture, is given by the expression (with the origin of the z axis at the focus):

$$A(x, y, -L) = \frac{1}{\sqrt{x^2 + y^2 + L^2}} \exp\left[-ik\sqrt{x^2 + y^2 + L^2}\right] \text{ for } \theta \leq \theta_{max} \qquad (1)$$

and

$$A(x, y, -L) = 0 \text{ for } \theta > \theta_{max} \qquad (2)$$

with $\tan(\theta) = \sqrt{x^2 + y^2} / L$ and θ_{max} the angle of the marginal ray that exits from the objective of NA = 1.2 ($\theta_{max} = 64.5°$).

2.3.3 2D scattering sample

Each scattering bead of radius r_{bead} deposited on the coverslip is considered as a 2D phase object (see Fig. 3). The corresponding phase distribution is a function of the radial distance r from the center, given by the expression, $\Delta\varphi(r) = \Delta\phi\sqrt{1-(r/r_{bead})^2}$, with $\Delta\phi = 2r_{bead}k_0(n_{bead} - n_{med})$, where k_0 is the wave vector of light in vacuum and n_{bead} and n_{med} are the refractive indices of the bead and its immersion medium (in practice water, so that n_{med} = 1.332) respectively.
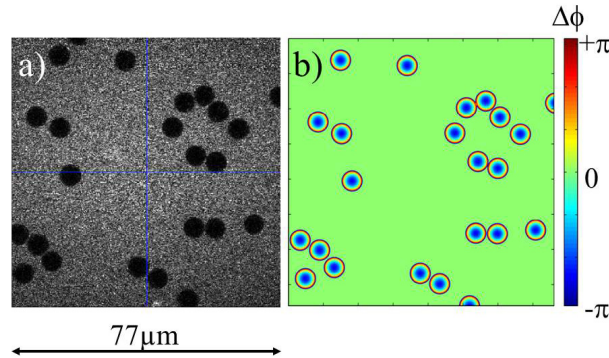

Fig. 3. a) Image of a sample of 6 µm silica beads deposited on a glass coverslip used for FCS measurements; b) Representation of the corresponding 2D phase object used in the numerical simulations

Specifying under which conditions a 3D object such as a spherical bead can be represented by a 2D phase object is not obvious. Comparisons of diffraction patterns calculated using the 2D phase object described above with an exact 3D Mie scattering calculation validate this 2D description provided that $\Delta\phi$ does not exceed a value of few

times π. Although this "flat" model describes well the wave at a large distance from the scattering substrate, it certainly fails at distances close to the size of the scattering beads. Moreover, as our numerical simulations compute the wave, propagated over a distance Z from the 2D phase object, the corresponding results are compared to the experimental ones at a distance $D = Z + 2r_{bead}$ from the coverglass surface.

Samples composed of beads located at random were generated. The points where the optical axis crosses the plane of this 2D model were chosen at random, although we have also excluded positions falling right on beads (in order to mimic the experimental protocol). In addition, actual configurations of beads were used in cases where we have accurately recorded both the image providing the positions of the beads and the location of the optical axis.

In all cases we obtained a synthetic 2D phase distributions $\Phi(x, y)$ representing the bead distribution, from which we generated the complex transmittance of the scattering layer, $T_\Phi(x, y) = \exp[i\Phi(x, y)]$, imparted on the incoming beam. The illumination intensity in the sample, $I_{ill}(x,y,z)$, was eventually calculated by propagating the transmitted wave so obtained.

2.3.4 Confocal detection

The spherical wave emitted from point $M(x_0,y_0,z_0)$ is given by:

$$A_{em}(x_0, y_0, z_0; x, y, z) = \frac{1}{\sqrt{(x - x_0)^2 + (y - y_0)^2 + (z + z_0)^2}}$$
$$\times \exp\left[ik\sqrt{(x - x_0)^2 + (y - y_0)^2 + (z + z_0)^2}\right] \tag{3}$$

Note the term $z + z_0$ (instead of $z - z_0$), which is consistent with the transmission geometry. Then, a phase object, identical to the one encountered by the illumination beam, transmits the emitted fluorescent wave that becomes $A_{em-tr}(x_0,y_0,z_0;x,y,z)$, before being collected by a replica of the objective and sent towards the detector. This collection process is described by a 2D complex transmittance, $T_{coll}(x,y)$, that applies to the fluorescent wave to give the collected wave, $A_{coll}(x,y,z) = A_{em-tr}(x_0,y_0,z_0;x,y,L) \times T_{coll}(x,y)$, that eventually propagates in the imaging space, where:

$$T_{coll}(x, y) = \exp\left[-2ik\sqrt{x^2 + y^2 + L^2}\right] \tag{4}$$

The collecting optics has a -1 magnification. In these conditions the focal point F is imaged at point F' symmetric of F with respect to the position of the collecting optics (Fig. 2). This means that $T_{coll}(x,y)$ reverses the radius of curvature of the spherical wave coming from F, so that it converges to F'. Note the -2 factor in the argument of the exponential of Eq. (4), instead of -1 for the focusing beam (Eq. (1).

In principle the computation of the Molecular Detection Function (MDF) is extremely tedious since, for each source point in the object space, it is necessary to calculate the fluorescence intensity distribution over the detector area. Fortunately it turns out that, in our case, the fluorescence intensity distribution after crossing the scattering substrate is the same wherever the source point is. In other words, isoplanatism still holds to some limit, which is also called the "memory effect" [18,19]. In addition, neglecting chromatic effects between the illumination and detection paths (the fluorophore used has a Stoke shift $\cong$ 25 nm), the intensity distribution of illumination is identical to that of the fluorescence. More precisely, the 3D fluorescence intensity at point $M'(x',y',z')$, emitted from source point $M(x_0,y_0,z_0)$, after crossing the scattering substrate and refocusing by the imaging optics is given by:

$$I_{fluo}(x_0, y_0, z_0; x', y', z') \propto I_{ill}(x_0 + x', y_0 + y', z_0 + z') \tag{5}$$

where the coordinates x', y', z' are relative to origin F'.

This reciprocity relationship is consistent with geometrical optics laws with -1 magnification. We have verified that this relation holds for x and y smaller or equal to 2 μm and for z smaller or equal to 5 μm. Since these limits are much larger than the size of the Point Spread Function, the above Eq. (5) is expected to be valid in practice for our numerical simulations. Finally, the detector being located in the image focal plane ($z' = 0$), the MDF that describes the fluorescence intensity signal collected for each molecule located at position x_0, y_0, z_0 can be expressed as:

$$MDF\left(x_0, y_0, z_0\right) \propto I_{ill}\left(x_0, y_0, z_0\right) \int_0^{r_{pin}} I_{ill}\left(x_0 + x', y_0 + y', z\right) dx' dy' \qquad (6)$$

where the integration is carried out over the area of the pinhole. Here the size of this pinhole corresponds to the experimental configuration, *i.e.* $r_{pin} = 0.2$ μm.

The last step consists in calculating the total count rate given by:

$$CR \propto \int MDF\left(x_0, y_0, z_0\right) dx_0 dy_0 dz_0 \qquad (7)$$

and the number of molecules as:

$$N \propto \left[\int MDF\left(x_0, y_0, z_0\right) dx_0 dy_0 dz_0\right]^2 / \int MDF^2\left(x_0, y_0, z_0\right) dx_0 dy_0 dz_0 \qquad (8)$$

2.3.5 Computational details

Most of the computations have been carried out using Matlab. The scalar angular spectrum model is implemented according to [20] on a 3000 × 3000 grid with a pitch of 0.05 μm. The illumination field is calculated for a series of 81 planes spaced by 0.08 μm. The *MDF* is then computed on a volume of 7.5 × 7.5 μm^2 (radial) by 6.4 μm (axial). Integrals of *MDF* and MDF^2 are then computed to yield the FCS metrics N and CR. Computation time for a given distance Z between the scattering substrate and the focus is a few minutes on a standard laptop. Statistics over the scattering substrate bead configurations have been obtained from the numerical simulations of 15 model samples. Computation of Mie scattering cross sections have been carried out using the Fortran code "CALLBH" given by Bohren and Huffmann [15].

3. Results and discussion

3.1 Results

Figure 4 shows the measured fluorescence count rate (*CR*) and number of molecules (*N*), as a function of the distance D between the focus and the scattering layer, for a series of samples of various surface densities, composed of silica beads of diameters 3, 6 and 15 μm and of PAA beads of diameter 14.5 μm. Several features appear immediately: for every series of samples, both CR/CR_0 and N/N_0 graphs exhibit similar shape (the 0 subscripts stand for the values with no scattering). The fluorescence count rate decreases with focus distance D from the scattering substrate and tends towards a non-zero constant at large D. The number of molecules first increases with D, reaches a maximum, then decreases and returns to a value close to N_0 at large distance D.
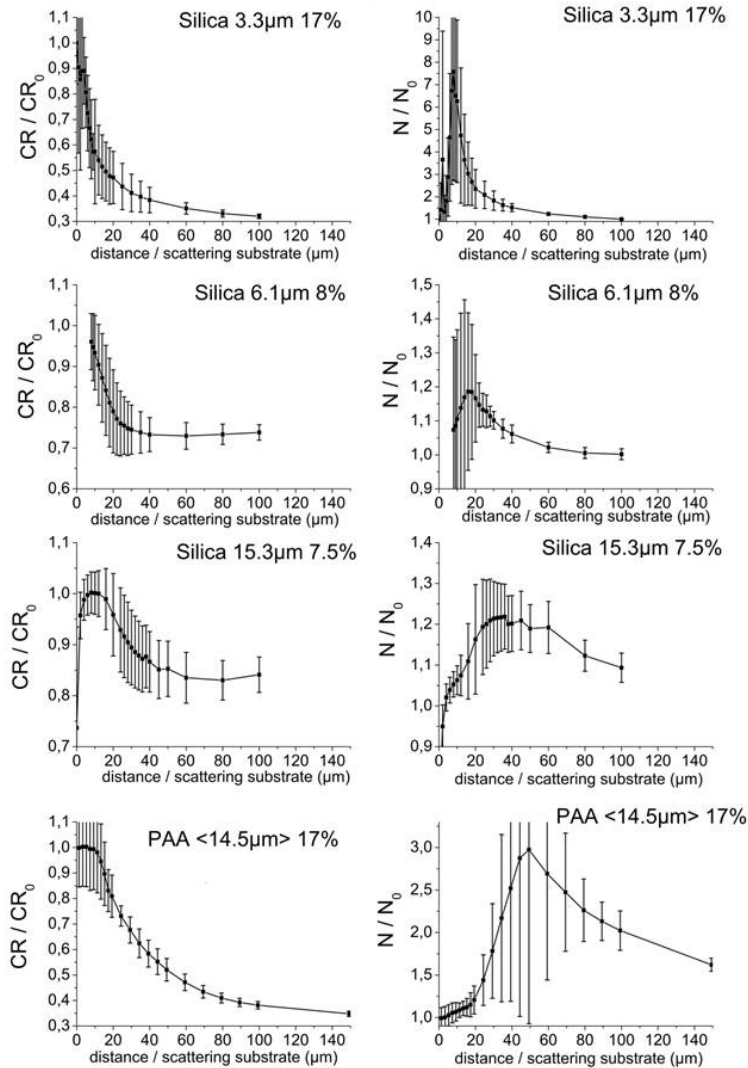
Fig. 4. FCS metrics (fluorescence count rate, CR and number of molecules, N) normalized to the value with no scattering substrate as a function of the distance D between the scattering substrate and the focus. Experimental values averaged over 18 configurations of 3 μm silica beads (average coverage fraction 17%), 16 configurations of 6 μm silica beads (average coverage fraction 8%), 19 configurations of 15 μm silica beads (average coverage fraction 7.5%) and 22 configurations of PAA beads of diameter 14.5 μm (average coverage fraction 17%). The error bars represent one standard deviation of the measurements.

Moreover, the shape of these graphs scales with the size of the beads, as shown in Fig. 5 where the graphs have been replotted with the horizontal axis scaled with respect to the size of the beads. Other measurements, made with sparse layers of latex beads of various diameter (data not shown), confirm this scaling with the size of the beads. This is one main point of our study that will be discussed below. In addition, it is worth to mention that for a given type of beads the amplitude of the variations of the FCS metrics increases with the coverage fraction of the scattering substrate, which is not surprising (data not shown). Finally we observe the large variability of the data that tends to be smaller at large D.
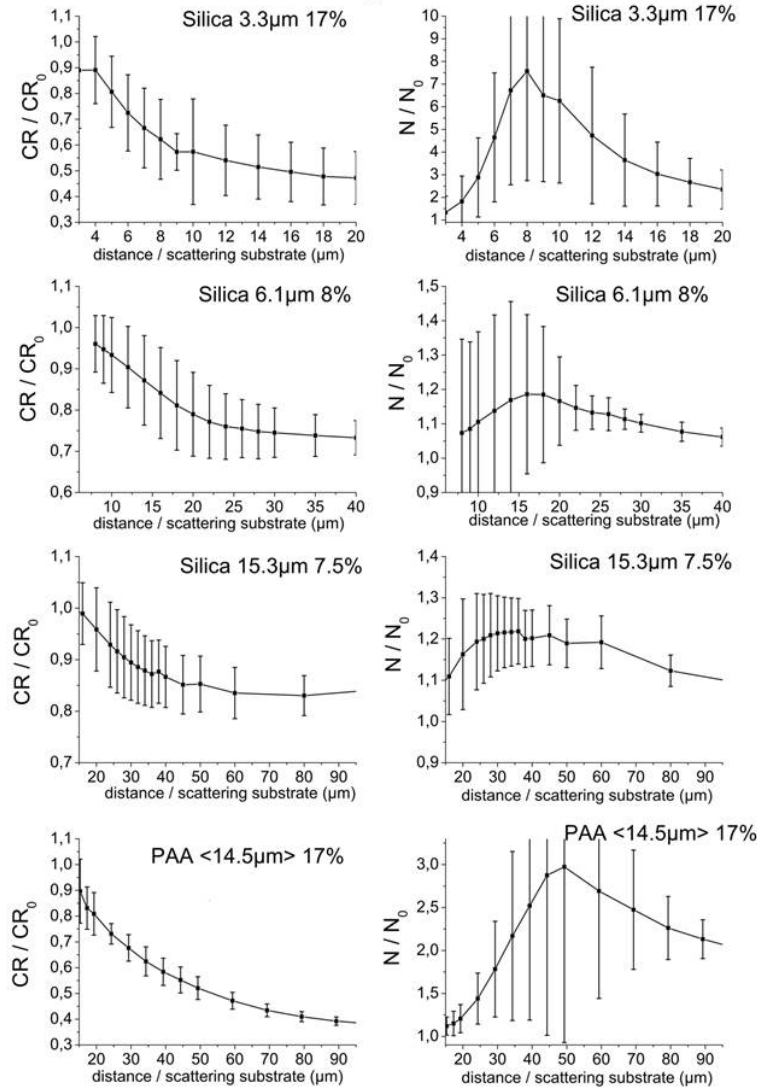
Fig. 5. Same as Fig. 4, but with the horizontal axis z scaled with respect to the size of the beads.

Figure 6 shows that all these features are reproduced by the numerical simulations, although the amplitude of the maximum value of the enlargement of the detection volume described by the N/N_0 curve seems to be underestimated in the simulations. It is likely that the difference between the measurements and the numerical simulations is due to our representation of the beads as "flat" 2D phase objects and that this assumption is not valid at small distances.
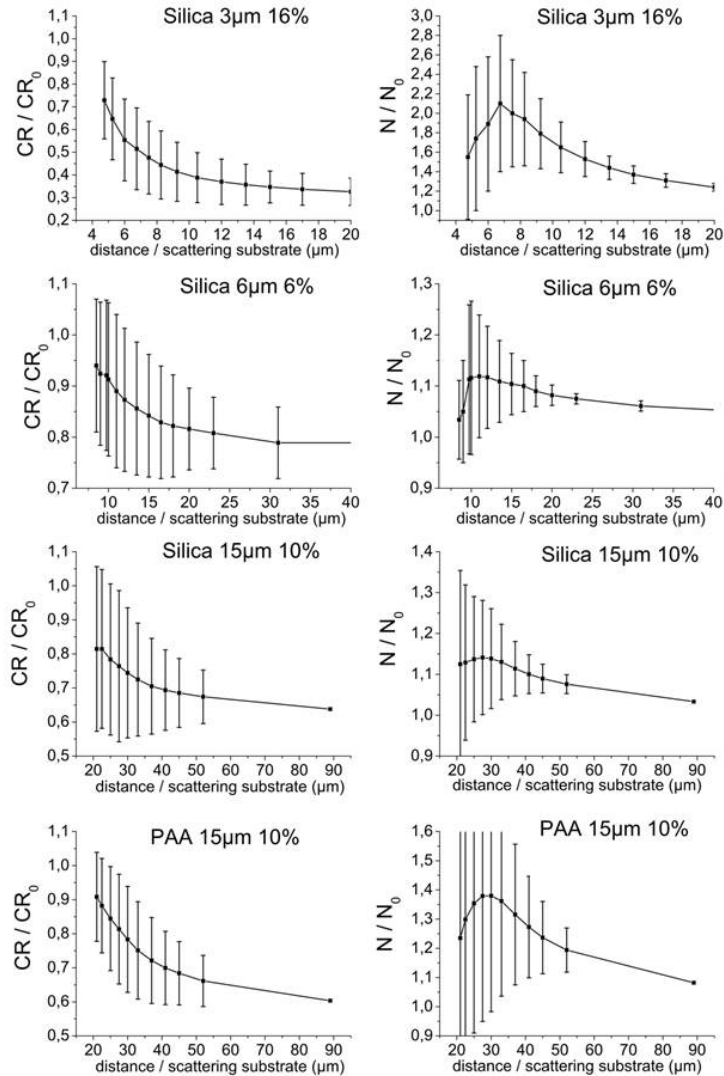
Fig. 6. Numerical simulations of FCS metrics (fluorescence count rate, CR and number of molecules, N) normalized to the value with no scattering substrate as a function of the distance D between the scattering substrate and the focus. The numerical simulations correspond to the conditions of Figs. 4, 5. The data are the result of an average over 15 random configurations; error bars represent one standard deviation.

The large variability in the data is due to the impact of the exact positions of the beads and to their distance from the objective axis. This can be seen in Fig. 7 that shows measurements (and the associated numerical simulations) for four configurations where both the bead and the optical axis positions have been recorded. These four configurations correspond to the same coverage fraction, which can be seen by the fact that all the graphs seem to merge at large distance D. However, at small distance they strongly differ, with a good agreement between the measurements and the numerical simulations.
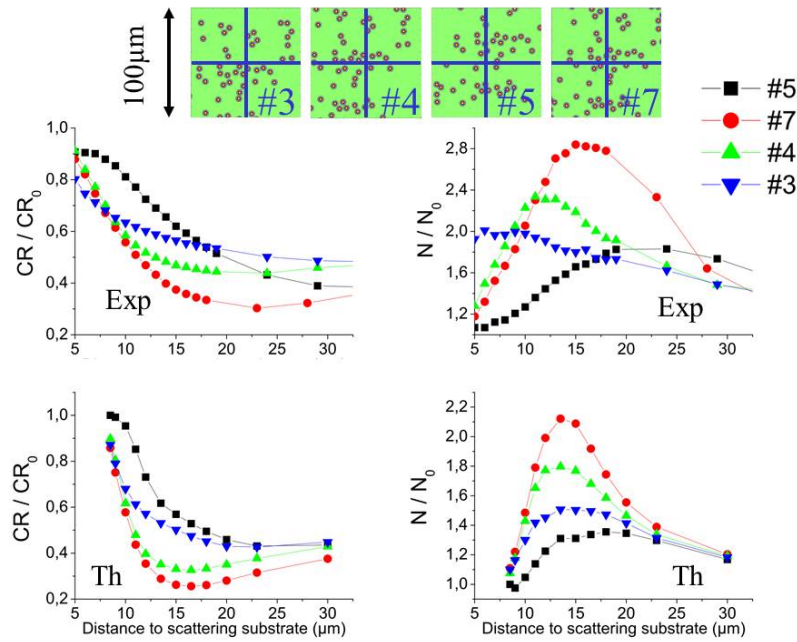
Fig. 7. Normalized FCS metrics (fluorescence count rate, CR and number of molecules, N), as a function of the distance D between the scattering substrate and the focus. The plots correspond to different configurations of the scattering substrate as shown on the top of the figure. Numerical simulations (bottom) refer to the same scattering substrate configurations as the measurements. The substrate is covered by 6 µm silica beads.

A simple and quantitative interpretation of these observations can be given in terms of local coverage fraction *cov* of the scattering substrate, defined by the bead areas within the area intercepted by the light beam focused by the objective. Given the numerical aperture NA = 1.2 of our optics, the radius of this circular area increases like $\cong 2D$. Figure 8 shows that for each configuration this local coverage fraction *cov* closely mimics the N/N_0 curves. Moreover the count rate curve CR/CR_0 can be correlated with the quantity $(1-q \times cov)^2$ where q is the Mie scattering efficiency of the beads as discussed below, the exponent 2 accounting for the fact that the scattering substrate is crossed twice by the light (illumination and fluorescence)
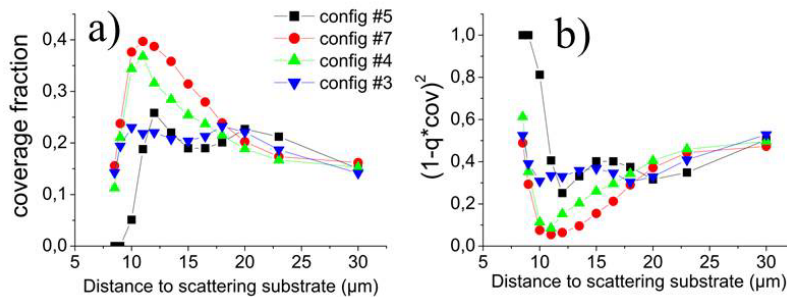

Fig. 8. a) Graph of the local coverage fraction, *cov*, of the optical beams (illumination and fluorescence) by the beads, corresponding to the configurations of Fig. 7; b) Graph of the quantity $(1-q \times cov)^2$, where q is the Mie scattering efficiency (see below, Fig. 10): this quantity correlates with the attenuation of the count rate displayed in Fig. 7.

3.2. Discussion

To summarize, we observe a monotonous decrease of the count rate when focusing deeper in the sample, while the number of molecules firstly increases at short distances, before recovering its unbiased value at distance large compared to the scatterers size. The phenomenon responsible for these observed effects is the scattering of light by the beads. As a result, part of the focused excitation beam is deviated and illuminates a region that extends beyond the focal region, inducing a fluorescence that is not detected. Similarly, due to light scattering in the backwards path, a fraction of the fluorescence excited by ballistic photons also cannot fall within the pinhole. The consequence of these effects can be seen in Fig. 9 that displays radial profiles of the calculated MDF in different planes at distances Δz from the focus. At axial distances smaller or equal to 0.5 µm, the absolute amplitude of the MDF in presence of beads is lower than the one in absence of scattering. Accordingly the scattering substrate tends to decrease the fluorescence count rate, which is the 3D integral of the MDF. However, an additional phenomenon can be observed in presence of light scattering. In planes out of focus (axial distances larger than 0.5 µm), the amplitude of the MDF radial profile relative to the maximum at focus becomes much higher, compared to the case without scattering beads. Hence, the MDF volume is longer and so is the number of molecules, N. In the particular case of Fig. 9, light scattering attenuates the count rate by a factor 2.5 and increases the size of the detection volume by 1.7.
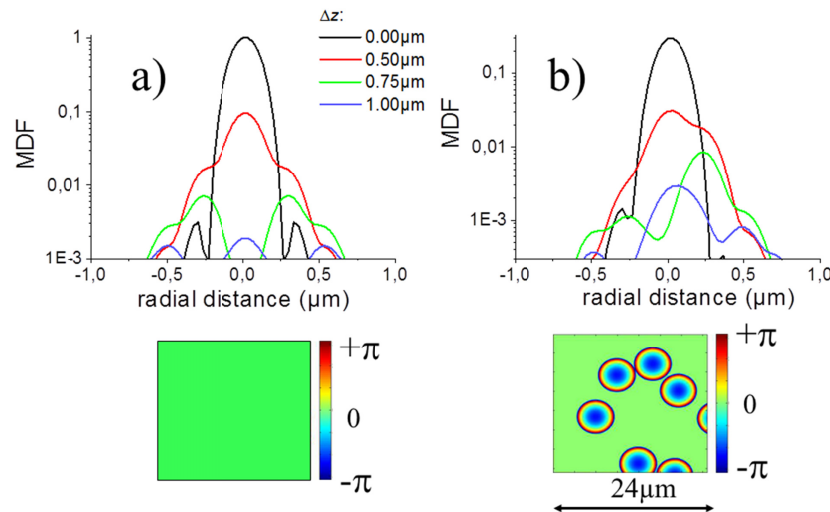

Fig. 9. Molecular Detection Function calculated using our numerical model. a) Without scattering beads, water immersion objective / NA = 1.2, λ_0 = 0.56 µm. b) With an aberrating phase object placed at distance corresponding to 12 µm from the focus. The phase distribution of the scattering object is represented below.

As the area illuminated by the scattered light increases like the square of the distance D from the scattering substrate, the pollution of the ballistic signal by molecules excited by this scattered light decreases with D. This explains why the relative detection volume represented by the quantity N/N_0 tends to 1 for large D, corresponding to the situation without the scattering substrate.

To discuss our observations more quantitatively, it is necessary to consider the quantities describing the scattering of light by a single spherical particle, namely Mie scattering. These quantities are the total scattering cross section, σ_{tot} and the differential scattering cross section, $d\sigma_{tot}/d\Omega$. It turns out that a very important physical parameter that determines the behavior of this scattering is the phase delay, $\Delta\phi = 2r_{bead}k_0\Delta n$, that is imparted to a light beam of wave

vector k_0 in vacuum, traveling through the center of a bead of radius r_{bead} and refractive index contrast Δn with the surrounding medium. First of all, let us consider the scattering efficiency q for a particle defined as the ratio of total cross section to the geometrical cross section, $q = \sigma_{tot}/\pi r_{bead}^2$. Figure 10 shows that for a wide range of physical parameters, r_{bead}, Δn and λ, this quantity is only a function of the phase delay $\Delta\phi$. While this behavior is predicted by the Rayleigh-Gans theory [15], it is expected to be valid for $\Delta\phi$ smaller than 1 [21]. Figure 10 indicates that the universal dependence of q with $\Delta\phi$ extends to $\Delta\phi > 1$. This function $q(\Delta\phi)$ vanishes to zero for small $\Delta\phi$ and tends to 2 for large $\Delta\phi$. Also, it shows an oscillatory behavior with a maximum that exceeds 3 for $\Delta\phi \cong \pi$.
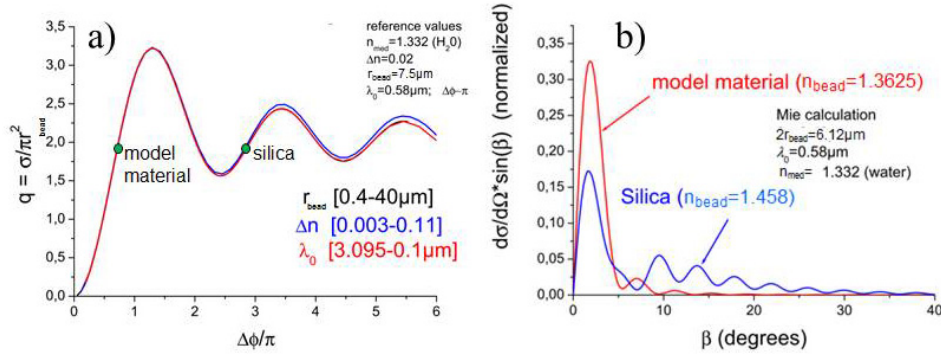

Fig. 10. Mie theory calculations of the total and differential scattering cross section. a) Scattering efficiency of light, q, by a spherical dielectric particle as a function of the phase delay $\Delta\phi$. Three plots are superimposed corresponding to the variation of $\Delta\phi$ induced by the variation of one of the three parameters r_{bead} (particle radius), Δn (refractive index contrast between the particle and the surrounding medium) and λ_0 (wavelength of light in vacuum). When one of these three parameters is varied, the others stay at the reference values. The two green dots correspond to two particles of same diameter (6.12 µm), but different refractive indices at $\lambda_0 = 0.56$ µm, 1.3625 for the model material and 1.458 for silica, such that they have the same scattering efficiency, $q = 1.94$. Their respective phase delays are 0.71π and 2.8π. b) Plots of the differential cross section vs the deflection angle for these two particles, averaged over polarizations and weighted by the sine of the scattering angle.

We suggest that this q peak corresponds to the crossover between two scattering regimes, as can be seen from the shape of the differential scattering cross section vs the scattering angle (Fig. 10), for two kinds of spherical particles having the same scattering efficiency q. One is a silica particle ($n_{bead} = 1.458$) of 6.12 µm immersed in water, interacting with a light beam of wavelength 0.56 µm in vacuum. This case corresponds to a relatively large phase delay, $\Delta\phi = 2.8\pi$. The second one is a model material particle of the same diameter, but with a refractive index $n_{bead} = 1.3625$ corresponding to a smaller phase delay $\Delta\phi = 0.71\pi$. Both have the same scattering efficiency $q = 1.94$, as shown in Fig. 10. As they also have the same diameter, the integral of both differential cross sections are the same. However, for the low refractive index particle, the curve shows only a single peak centered at the value given by the diffraction angle $\beta_{diff} \sim \lambda_0/r_{bead}$. In contrast, for the silica particle of larger refractive index we still observe a first peak at $\beta_{diffract}$, but with half amplitude. Additionally, there is a broad oscillating bump, which contribution to the total scattering cross section is about the same as the first peak, though it spreads over a relatively wide angular range. We interpret these two contributions as being due to diffraction and refraction, respectively. In the first case, the deflection angle depends only upon the particle size, while in the second case it is determined by the refractive index contrast. These two contributions have the same magnitude for large $\Delta\phi$ (e.g. 2.8π), while they merge for $\Delta\phi \lesssim \pi$ (e.g. 0.71π). For smaller $\Delta\phi$, only the diffraction contribution is left, but its magnitude tends to zero when $\Delta\phi$ vanishes ($\Delta n \to 0$).

We now come back to the effect of light scattering on FCS measurements with silica beads. We suggest that the diffraction part of the differential scattering cross section, *i.e.* the peak at low deflection angle $\beta_{diff} \sim \lambda_0/r_{bead}$, is mostly responsible for the broadening of the detection volume. The refraction part is associated with deflection angles large enough so that the corresponding fluorescence light is blocked by the confocal pinhole. The diffraction part of the scattered light forms a spot at distance D whose radius is about $\beta_{diff} \times D$. The distance D_{max} between the scattering substrate and the focus where the detection volume broadening effect is maximum corresponds roughly to the situation where the diffracted light spot radius is about the size of the point spread function at the focus, *i.e.* $\beta_{diff} \times D_{max} \sim \lambda_0/NA$, or $D_{max} \sim r_{bead}/NA$. Of course this relationship is very approximate, but it explains the scaling with the size of the scattering particles that can be seen in Figs. 4-6. It also indicates that the distance at which the broadening effect is maximum increases when the objective numerical aperture decreases, which is confirmed by numerical simulations (data not shown).

Following these considerations, the maximum broadening of the detection volume observed at D_{max} should be especially large for scattering substrates composed of particles with $\Delta\phi \sim \pi$ because of their large scattering efficiency (see Fig. 10). Such a situation is achieved with the 3 µm silica particles characterized by $\Delta\phi = 1.4\pi$ and $q = 3.2$. As a matter of fact, Fig. 4 shows that the detection volume broadening is particularly large in this case, in agreement with numerical simulations (Fig. 6). A similar situation is observed with PAA particles, although their refractive index ($n_{PAA} \cong 1.349$) is much closer to the one of the surrounding medium (water, $n_{med} = 1.332$), compared to the silica case. However, the combination of this very small refractive index contrast ($\Delta n = 0.017$) with their relatively large diameter (14.5µm) corresponds to $\Delta\phi = 0.9\pi$ and $q = 2.51$. Once again, as expected, Figs. 4 and 6 show that the detection volume broadening is large in this case.

Finally, it is important to comment about the value of the attenuation of the count rate. At small distance D between the focus and the scattering substrate its value is quite sensitive to the configuration of the beads, as we have seen. This is due to the fact that the number of beads intercepted by the light beam is small, inducing large relative fluctuations of the number of beads. At the same time, the distortion of the light beam is sensitive to the exact location of the beads. However, at large D, for all configurations with the same value of the coverage fraction, the count rate tends to the same asymptotic limit that corresponds to the remaining ballistic light. We thus expect the asymptotic value to scale as:

$$\left(\frac{CR}{CR_0}\right)_{D\to\infty} \approx (1 - q \times cov)^2 \qquad (9)$$

where cov is the average coverage fraction of the scattering substrate and q is the scattering efficiency of the beads (see Table 1).

Table 1. Correlation of the Mie scattering efficiency and coverage fraction with asymptotic count rate

Beads	Mie scattering efficiency q	coverage fraction cov	$(1-q \times cov)^2$	CR/CR_0 measured
Silica 3 µm	3.24	0.17	0.2	0.32 ± 0.01
Silica 6 µm	1.93	0.08	0.72	0.74 ± 0.02
Silica 15 µm	2.03	0.075	0.72	0.84 ± 0.04
PAA <14.5> µm	2.51	0.17	0.33	0.35 ± 0.01

The exponent 2 accounts for the fact that the scattering substrate is crossed twice, i.e. by the excitation and fluorescence light. This relationship suggests that there is no more ballistic light when the coverage fraction exceeds a value of $1/q$, *i.e.* typically 50%.

4. Conclusion

In the present work, we have investigated, experimentally and theoretically, the parameters that affect a FCS signal measured with a confocal microscope through a 2D substrate of spherical scattering particles. These parameters are the particle size, the phase delay of the light through its center compared to the surrounding medium, the coverage fraction of the substrate by the particles and the measurement depth behind the substrate.

The size of the particles determines the average distance at which the broadening of the detection volume is largest. Thus, the bias of the quantities measured by FCS, namely number of molecules and diffusion time, are mostly impaired at that position. This distance does not depend on the refractive index of the particles.

The amplitude of this bias is determined by the phase delay $\Delta\phi$ (depending on the refractive index of the particles) and is maximum for $\Delta\phi \sim \pi$. For particles of about 10 μm in diameter, this corresponds to a fairly low refractive index contrast compared to a surrounding medium like water, which are conditions typical of biological cells. These effects increase with coverage fraction and may be very strong even for moderate coverage fractions (30%).

At distances large compared to the size of the particles, the detection volume recovers its unbiased value (together with the diffusion time). This result seems to contradict the "shower curtain effect" [22,23] where the image contrast is known to decrease as the distance between the object and the scattering layer increases. Actually, to observe a "shower curtain effect" the scattering of light must be total, *i.e.* no more ballistic light. In contrast, our scattering substrates are sparse and transmit some ballistic light. As a result, the FCS signal detected at large distance corresponds to this remaining ballistic light, inducing a fluorescence signal attenuated by a factor that involves the coverage fraction times the scattering efficiency of the particles. Conversely, if light was totally scattered, we would enter a regime of fully developed speckle where standard FCS would no longer be possible, regardless of the distance to the substrate.

Although the current analysis is restricted to a simple 2D scattering substrate composed of identical spherical particles, we have also tackled the case of living cells platted on a cover slide (data not shown). We have observed a monotonous decrease of the signal down to a constant value at large distances. However, as there is a continuous distribution of scattering objects, the number of molecules does not exhibit a maximum and reaches an upper plateau. Situations of much more practical interest involve thick, inhomogeneous, scattering media. It would be interesting to apply our considerations to these situations and this will be the subject of further studies. At this point, we infer that structures closest to the focal point are mostly responsible for the distortion and broadening of the detection volume, while more distant structures contribute to the attenuation of the fluorescence signal. Moreover, large structures with small refractive index contrast may induce strong aberrations, while small structures induce scattering at large angles which is blocked by the confocal pinhole.

References

1. E. Haustein and P. Schwille, "Fluorescence correlation spectroscopy: novel variations of an established technique," Annu. Rev. Biophys. Biomol. Struct. **36**(1), 151–169 (2007).
2. E. L. Elson, "Quick tour of fluorescence correlation spectroscopy from its inception," J. Biomed. Opt. **9**(5), 857–864 (2004).

3. J. Enderlein, I. Gregor, D. Patra, T. Dertinger, and U. B. Kaupp, "Performance of fluorescence correlation spectroscopy for measuring diffusion and concentration," ChemPhysChem **6**(11), 2324–2336 (2005).
4. C.-E. Leroux, A. Grichine, I. Wang, and A. Delon, "Correction of cell-induced optical aberrations in a fluorescence fluctuation microscope," Opt. Lett. **38**(14), 2401–2403 (2013).
5. C.-E. Leroux, S. Monnier, I. Wang, G. Cappello, and A. Delon, "Fluorescent correlation spectroscopy measurements with adaptive optics in the intercellular space of spheroids," Biomed. Opt. Express **5**(10), 3730–3738 (2014).
6. S. Zustiak, J. Riley, H. Boukari, A. Gandjbakhche, and R. Nossal, "Effects of multiple scattering on fluorescence correlation spectroscopy measurements of particles moving within optically dense media," J. Biomed. Opt. **17**(12), 125004 (2012).
7. C. M. Blanca and C. Saloma, "Monte carlo analysis of two-photon fluorescence imaging through a scattering medium," Appl. Opt. **37**(34), 8092–8102 (1998).
8. C. K. Hayakawa, E. O. Potma, and V. Venugopalan, "Electric field Monte Carlo simulations of focal field distributions produced by tightly focused laser beams in tissues," Biomed. Opt. Express **2**(2), 278–290 (2011).
9. Y. Chen, D. Wang, and J. T. C. Liu, "Assessing the tissue-imaging performance of confocal microscope architectures via Monte Carlo simulations," Opt. Lett. **37**(21), 4495–4497 (2012).
10. S. Y. Lee and M. A. Mycek, "Hybrid Monte Carlo simulation with ray tracing for fluorescence measurements in turbid media," Opt. Lett. **43**(16), 3846–3849 (2018).
11. B. H. Hokr, J. N. Bixler, G. Elpers, B. Zollars, R. J. Thomas, V. V. Yakovlev, and M. O. Scully, "Modeling focusing Gaussian beams in a turbid medium with Monte Carlo simulations," Opt. Express **23**(7), 8699–8705 (2015).
12. J. C. Ranasinghesagara, C. K. Hayakawa, M. A. Davis, A. K. Dunn, E. O. Potma, and V. Venugopalan, "Rapid computation of the amplitude and phase of tightly focused optical fields distorted by scattering particles," J. Opt. Soc. Am. A **31**(7), 1520–1530 (2014).
13. M. L. Byron and E. A. Variano, "Refractive-index-matched hydrogel materials for measuring flow-structure interactions," Exp. Fluids **54**(2), 1456 (2013).
14. F. Ingremeau, M. E. Dolega, J. Gallagher, I. Wang, G. Cappello, and A. Delon, "Optical sensing of mechanical pressure based on diffusion measurement in polyacrylamide cell-like barometers," Soft Matter **13**(23), 4210–4213 (2017).
15. C. F. Bohren and D. R. Huffmann, *Absorption and Scattering of Light by Small particles* (Wiley, 2007)
16. B. Richards, E. Wolf, and D. Gabor, "Electromagnetic diffraction in optical systems II. Structure of the image field in an aplanatic system," Proc. R. Soc. Lond. A Math. Phys. Sci. **253**(1274), 358–379 (1959).
17. L. Novotny and B. Hecht, *Principles of Nano-Optics* (Cambridge University Press, 2012).
18. I. Freund, M. Rosenbluh, and S. Feng, "Memory effects in propagation of optical waves through disordered media," Phys. Rev. Lett. **61**(20), 2328–2331 (1988).
19. S. Schott, J. Bertolotti, J.-F. Léger, L. Bourdieu, and S. Gigan, "Characterization of the angular memory effect of scattered light in biological tissues," Opt. Express **23**(10), 13505–13516 (2015).
20. Physics Forum, "Code of the Angular Spectrum Method," https://www.physicsforums.com/threads/code-of-the-angular-spectrum-method.823494/
21. M. Kerker, W. A. Farone, and E. Matijevic, "Applicability of Rayleigh-Gans Scattering to Spherical Particles," J. Opt. Soc. Am. **53**(6), 758–759 (1963).
22. Y. Kuga and A. Ishimaru, "Modulation transfer function of layered inhomogeneous random media using the small-angle approximation," Appl. Opt. **25**(23), 4382–4385 (1986).
23. E. Edrei and G. Scarcelli, "Optical imaging through dynamic turbid media using the Fourier-domain shower-curtain effect," Optica **3**(1), 71–74 (2016).